ANNALS OF GEOPHYSICS, VV, NV, PPPP, YYYY; doi:10.4401/ag-xxxx OPEN ACCESS

Source Characteristics of the Mw 4.3 and Mw 4.4 central San José Earthquakes Derived from Empirical Green's Functions

Aaron Moya (https://orcid.org/0009-0008-8834-4954)

(1) Laboratorio de Ingeniería Sísmica, Universidad de Costa Rica, Costa Rica

Article history: received Month DD, YYYY; accepted Month DD, YYYY

Abstract

We investigated the source characteristics of the August 22, 2025 (Mw 4.3) and January 19, 2026 (Mw 4.4) San José earthquakes. Although moderate in magnitude, both events occurred at a shallow depth (~4.0 km) beneath the central urban area of the capital city. They produced strong ground shaking with peak ground accelerations reaching approximately 230 gal. Using small aftershocks as Empirical Green's function (EGFs), we estimated the size of the strong-motion generation areas (SMGAs), rise time, rupture velocity, and associated stress drop for each event. Despite their similar magnitudes, the two earthquakes exhibit notable differences in SMGA size and stress drop, which appear to control the spatial distribution of observed acceleration.

Keywords: strong motion generation area; fault; accelerograph; earthquake; stress drop

1. Introduction

Urban areas located in tectonically active regions face a particular risk from earthquakes due to high population density and concentration of critical infrastructure. Understanding seismic hazard in such environments is therefore essential for effective risk mitigation and urban planning, particularly where active faults are poorly expressed at the surface or remain insufficiently studied. The capital city of Costa Rica, San José, is of particular interest in this sense because the urban development has often outpaced detailed seismotectonic investigations (Peraldo and Montero, 1999; Climent et al., 2008).

Although the country lies within a highly active tectonic setting controlled by the interaction of the Cocos, Caribbean, and Panama microplates, no major active faults have been clearly identified directly beneath San José, or they remain poorly constrained (Fernández & Montero, 2002). Nevertheless, historical

and instrumental seismicity demonstrates that the Greater Metropolitan Area (GAM) is exposed to significant earthquake hazard (Hidalgo-Leiva et al., 2022; Benito et al., 2025).

Historical seismicity reveals the potential consequences of earthquakes in the GAM. The most damaging event was the Ms 6.4 Cartago earthquaka of May 4, 1910 (IMM VIII). It devastated the city of Cartago, located approximately 20 km east of San José. Intensity studies and historical accounts indicate near-total destruction of the city and approximately 700 fatalities, making it the most disastrous earthquake in Costa Rican history (Montero & Miyamura, 1981; Peraldo & Montero, 1999; Alonso-Henar et al., 2013). This event serves as a clear reminder of the catastrophic impact that a shallow crustal earthquake can have on urban centers.

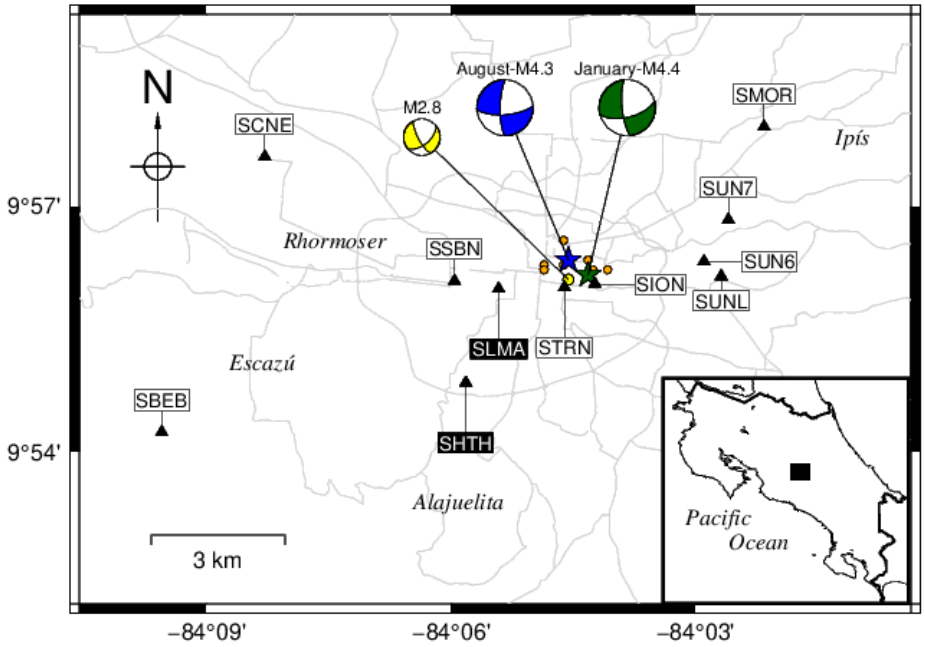

Figure 1. Seismicity recorded in central San José, Costa Rica from August, 2025 until January, 2026. The map shows the epicentral locations of the two significant events: the August 22, 2025 (Mw 4.3) (blue star) and the January 19, 2026 (Mw 4.4) (green star). The yellow circle shows the August 22, 2025 Mw 2.8 event used as empirical Green's function (EGF). Orange circles correspond to recorded aftershocks. Gray lines correspond to mayor roads. Focal mechanism solutions indicate a predominance of left-lateral strike-slip faulting. Black triangles show the location of the strong motion stations used in this study. SHTH and SLMA were not part of the EGF analysis. The inset map highlights the study area within Costa Rica..

The most recent Mw 6.1–6.2 Cinchona earthquake of January 8, 2009, located approximately 30–40 km north-northwest of San José (Barquero, 2009) shook San José violently. A station located some 13-14 km away from the epicenter recorded a value of 658 gals and 26.5 cm/s. This shallow, oblique-slip event generated strong ground shaking and extensive landslides, particularly on the steep volcanic slopes near the epicentral area (Quesada-Román & Barrantes-Castillo, 2016). Estimates from the Comisión Nacional de

Emergencias (CNE) and national media indicate around 25–27 confirmed deaths, at least five missing, and approximately 100 injured, with hundreds of people displaced or sheltering in emergency accommodations after structural failures and slope collapses blocked access routes and damaged homes. More than 2,300 structures were damaged, with nearly 800 destroyed.

In this context, the earthquakes that took place on August 22, 2025 and January 19, 2026, directly beneath the city of San José, provide a particularly informative case study (Fig. 1). The Laboratorio de Ingeniería Sísmica at the Universidad de Costa Rica (LISUCR) estimated the magnitudes as Mw 4.3 and Mw 4.4 for the first and second events, respectively. The Red Sismológica Nacional (RSN, Universidad de Costa Rica) reported slightly higher magnitudes of Mw 4.4 and Mw 4.5, while the Observatorio Vulcanológico y Sismológico de Costa Rica (OVSICORI-UNA, Universidad Nacional) estimated their magnitude as Ml 4.1 and Ml 4.4 respectively. Despite the small differences, all three institutions consistently indicated that the first event was smaller than the second one.

Those events and some of their aftershocks were recorded by a dense strong-motion network deployed by the LISUCR across the city (Fig. 1). This allowed for high-resolution observations of near-source ground motions close to the source area. Despite their moderate magnitude, each earthquake produced notable peak ground accelerations (PGA) and velocities (PGV) throughout the GAM as shown in Figure 2. The largest PGA and PGV values are systematically observed at stations located east of the epicenter.

In this analysis, we apply an empirical Green's function (EGF) approach using a nearby small aftershock, Mw 2.8, with similar focal mechanism and hypocentral location as the M4+ events (Fig. 1). The focal mechanism was determined by the LISUCR using the P-wave polarities and the method proposed by Hardebeck & Shearer (2002). The use EGF method allows for the removal of the unknown path and site effects from the observed waveforms, thereby isolating the source time function and rupture characteristics of the main event such as the stress drop, rupture velocity, and rise time.

2. Data and Methods

2.1 Strong Motion Data

The LISUCR maintains a nationwide network of strong-motion instruments that provide continuous records of ground motion from moderate to large earthquakes (Moya et al., 2020). These instruments are located at a variety of sites, and within the GAM there are several dozen stations, including installations in

high-rise buildings. Figure 3 shows the distribution of the strong-motion stations. Black triangles correspond to stations used to compute the focal mechanisms in this study.

Focal mechanisms were determined using the HASH algorithm (Hardebeck & Shearer, 2002) based on first-motion polarity data. The Mw 2.8 event is constrained by 28 polarity observations, the Mw 4.3 event by 23 polarities, and the Mw 4.4 event by 30 polarities. The station distribution provides generally good azimuthal coverage as shown by Figure 3 with values of 0.928, 0.876, and 0.978 for the Mw 2.8, Mw 4.3 and, Mw 4.4 events. The preferred focal mechanism solutions are characterized by low polarity misfit, with values of 6.3%, 4.2%, and 11.3% for the Mw 2.8, Mw 4.3, and Mw 4.4 events, respectively. The corresponding HASH quality grades are B, A, and B which indicate moderate to well-constrained solutions for the purpose of the present study.

Earthquake locations were determined using the non-linear location algorithm NonLinLoc (Lomax et al., 2000). Location uncertainties are quantified by the 68% confidence ellipsoids. For the Mw 2.8 event, the semi-major, intermediate, and minor axes of the confidence ellipsoid are 0.97 km, 0.54 km, and 0.55 km, respectively. For the Mw 4.3 event, the corresponding values are 0.77 km, 0.53 km, and 0.42 km, and for the Mw 4.4 event they are 0.80 km, 0.49 km, and 0.53 km. These results indicate that location uncertainties are generally on the order of ~0.4–1.0 km which are small relative to the spatial separation between events.

Moment magnitude (Mw) was estimated from low-frequency displacement amplitude spectra following the procedure described in Moya (2024). Spectra were computed for multiple stations, and Mw was obtained from the average spectral level in the low-frequency plateau.

The network comprises a combination of force-balance accelerometers (FBA) and micro-electromechanical system (MEMS) sensors. FBA sensors are characterized by a wide dynamic range and low self-noise, which allow for reliable integration of acceleration records to velocity and displacement. In contrast, although MEMS sensors provide a cost-effective solution for dense urban deployments and perform adequately for moderate to large ground motions, their higher noise levels limit their ability to accurately capture low-amplitude signals from small events.

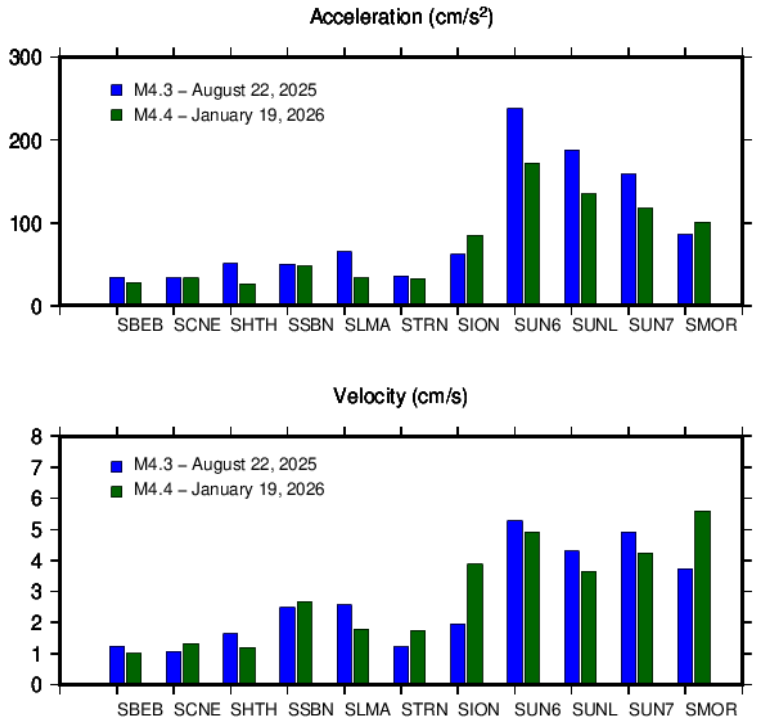

Figure 2. Maximum acceleration and velocity values recorded for the Mw 4.3 and Mw 4.4 events. The data are ordered from West to East by station code. The values highlight the spatial distribution relative to the hypocenter located between stations STRN and SION.

This limitation is particularly relevant for the candiate aftershocks used as EGFs in the present study (Table 1) and has two main implications. First, the frequency range of the analysis was restricted to 0.3–10.0 Hz due to the signal-to-noise ratio. Second, two of the eleven stations in the network—highlighted in black in Figure 1 and equipped with MEMS sensors—were excluded from the EGF analysis due to unstable integrated displacement waveforms. They were used only to extract the PGV and PGA paramters from the M4+ eventos that are shown in Figure 2.

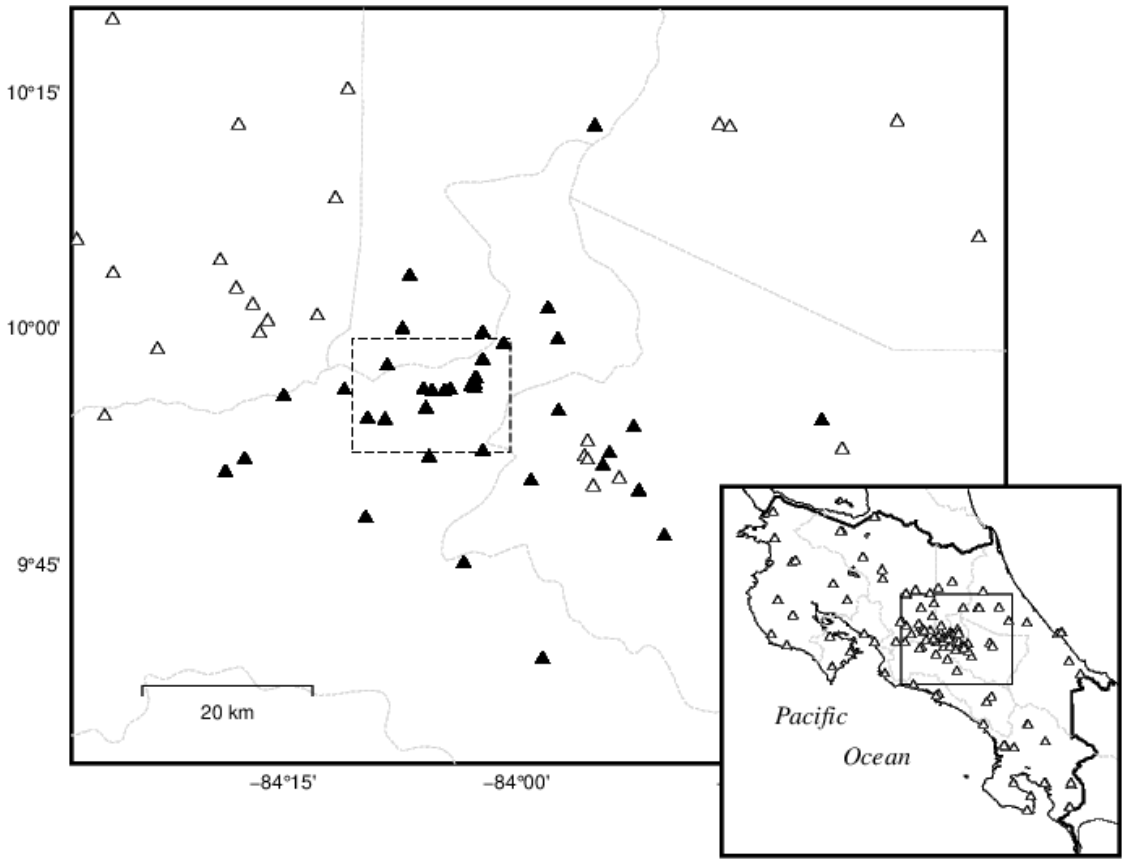

Figure 3. Strong motion station distribution throught Costa Rica. The dashed black box correspond to the study area shown in Fig 1. Dashed light gray lines correspond to provinces

Several aftershocks were evaluated as potential EGFs based on hypocentral proximity, focal mechanims, and magnitude. As shown in Table 1, the candidate events display consistent peak ground acceleration (PGA) values across stations, with similar relative amplitudes. However, events with magnitude M3.5 were not considered suitable EGFs because their source dimensions are not sufficiently small relative to the mainshocks we were simulating. On the other hand, the smallest events (M2.4–M2.6) exhibit low PGA values at several stations, approaching the noise level, which reduces their reliability as stable Green's functions, particularly when the double integration is done to compare displacement waveforms and for distant stations (i.e. SCNE, SBEB). Event number two which source parameters are listed in Table 2 was the best choice.

Table 1. Magnitude, depth (in km) and horizontal PGA values (in gals) at given stations for EGF candidates.

Candidate EGF	Mw	Depth	SBEB	SCNE	SION	SMOR	SSBN	STRN	SUNL	SUN6	
1	2.6	5.0	2.37	0.72	1.41	0.90	0.79	0.70	1.32	2.02	1.80
2	2.8	3.9	3.04	1.51	2.21	1.91	2.55	1.50	5.45	3.03	2.98
3	3.5	3.9	10.47	7.20	12.10	7.81	12.52	6.34	8.77	7.86	8.77
4	2.6	4.4	2.77	0.91	2.38	0.64	1.17	0.75	0.76	0.85	0.45

5	2.8	3.1	1.53	1.18	2.23	1.09	1.60	1.06	0.75	1.11	1.24
6	2.7	5.5	1.60	1.12	0.80	0.91	0.80	0.42	2.50	2.53	1.73
7	2.4	5.2	3.06	0.94	0.71	0.91	1.03	0.38	1.48	1.65	1.17
8	2.9	4.1	4.42	- - - -	5.58	4.37	2.60	- - - -	2.31	2.15	6.54
9	3.5	3.6	6.45	12.31	21.50	- - - -	9.12	- - - -	21.67	- - - -	24.60

To evaluate the quality of the EGF and mainshock events, we computed the signal-to-noise ratio (SNR) on one of the horizontal components (NS) for each station. The SNR is defined as the ratio of the RMS amplitude in the signal window to that in a pre-event or post-event noise window. In this case we used a 10s time-window. Waveforms were detrended, demeaned, and bandpass filtered between 0.1 and 10 Hz prior to calculation. The values are listed in Table 2. For the Mw 2.8 EGF candidate, SNR values across stations range from 42 to 165, with a mean of 99 ± 36. As expected, the larger events (Mw 4.3 and 4.4) show higher SNR values (mean 145 ± 72 and 106 ± 9, respectively), consistent with their stronger signal amplitudes.

Table 2. Signal to noise ratio (SNR) for selected events at each station.

Event	SBEB	SCNE	SION	SMOR	SSBN	STRN	SUNL	SUN6	SUN7	Mean ± Std
Mw 2.8	165	60	42	90	102	56	107	100	118	99 ± 36
Mw 4.3	293	83	103	128	165	106	193	77	217	145 ± 72
Mw 4.4	107	84	103	118	124	103	99	92	113	106 ± 9

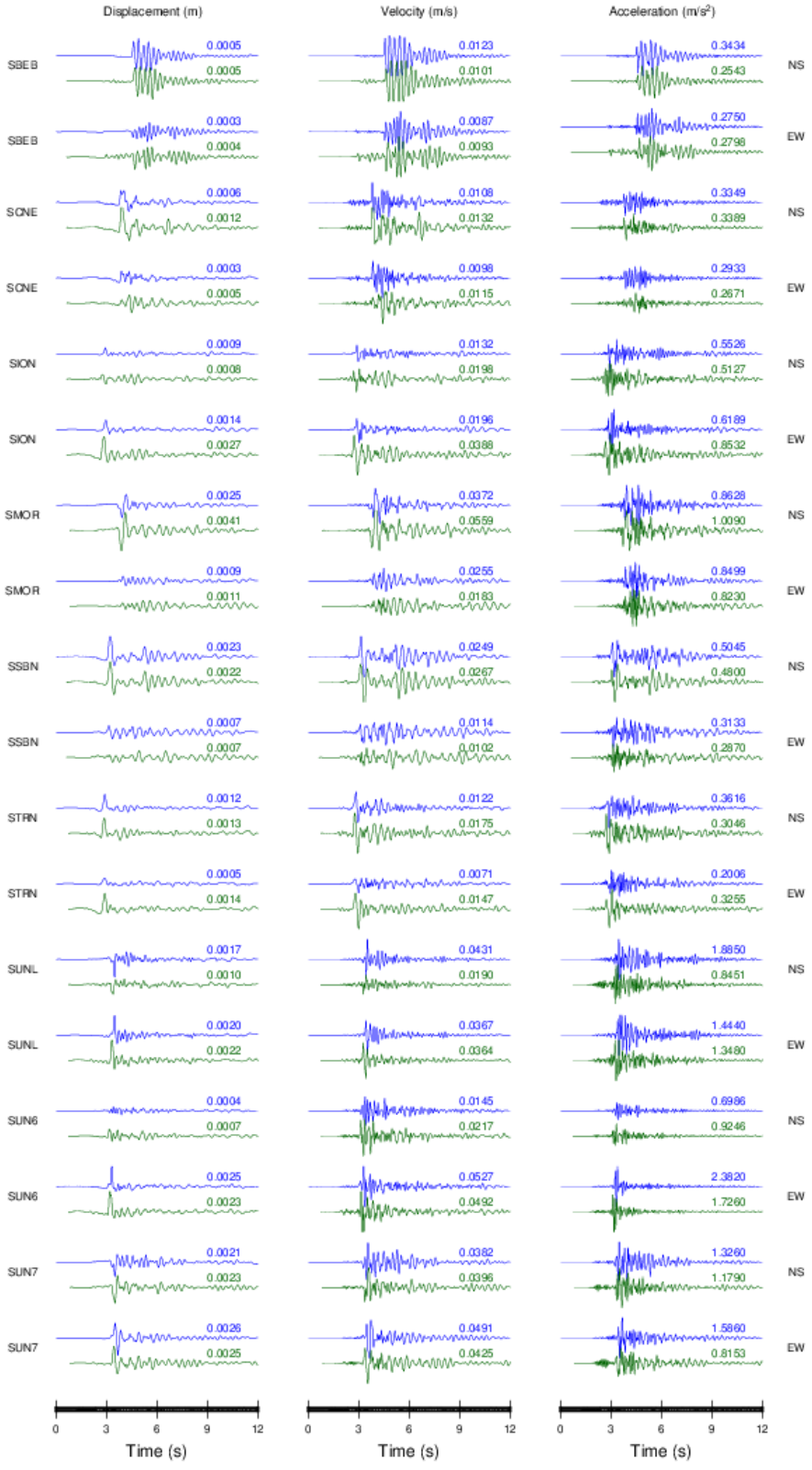

142 **Figure 3.** Observed displacement, velocity, and acceleration waveforms for the Mw 4.3 (blue) and Mw 4.4 (green) events.

143 Figure 3 shows the observed displacement, velocity, and acceleration waveforms for the Mw 4.3
144 (blue trace) and the Mw 4.4 (green trace) events. For both earthquakes, the waveforms exhibit clear, impulsive
145 onsets across the network, indicating good signal quality at the selected FBA stations. In the Mw 4.3 event,
146 the observed displacement records are characterized by relatively small peak amplitudes and short signal

durations, with most of the energy concentrated within the first few seconds following the initial arrival. The corresponding velocity waveforms show well-defined pulses with peak values generally below a few cm/s, while acceleration records display sharp, high-frequency content with distinct peaks and rapid decays. PGA values range from approximately 30–40 cm/s^2 at western stations such as SBEB and SCNE to more than 200–230 cm/s^2 at eastern stations including SUN6, SUN7, and SUNL.

Waveforms from the Mw 4.4 event display broadly similar characteristics, although displacement records show slightly longer durations and have larger peak amplitudes at several stations (e.g., SUNL, SCNE and SION). Despite the slightly larger magnitude of this event and its closer proximity to several eastern stations, the observed PGA and PGV values are not consistently larger than those of the Mw 4.3 earthquake.

Peak ground motion measurements summarized in Figure 2 reveal a pronounced azimuthal dependence in shaking intensity for both events. Stations located east of the epicenter record systematically larger PGA and PGV values than stations at comparable distances to the west, whereas western and more distant stations (e.g., SBEB and SCNE) show lower amplitudes and smoother waveform shapes. This spatial pattern is consistent across both mainshocks and is evident in both acceleration and velocity observations.

Normalizing peak ground motions by distance further emphasizes this azimuthal asymmetry (Fig. 4). Eastern stations (azimuths 60–120) exhibit PGA/R and PGV/R values that are 5–10 times larger than those observed at western stations (azimuths 240–300). The persistence of this contrast across multiple stations and for both events suggests that the observed amplitude enhancement cannot be explained solely by distance effects or site amplification.

The strong similarity of observed waveforms across the network suggests that the two earthquakes likely ruptured the same fault or fault segment, consistent with their similar focal mechanisms and hypocentral locations (Fig. 1. and Table 1). At the same time, systematic differences in amplitude, duration, and relative peak ground motions imply that the rupture processes were not identical, potentially reflecting variations related to the rupture processes.

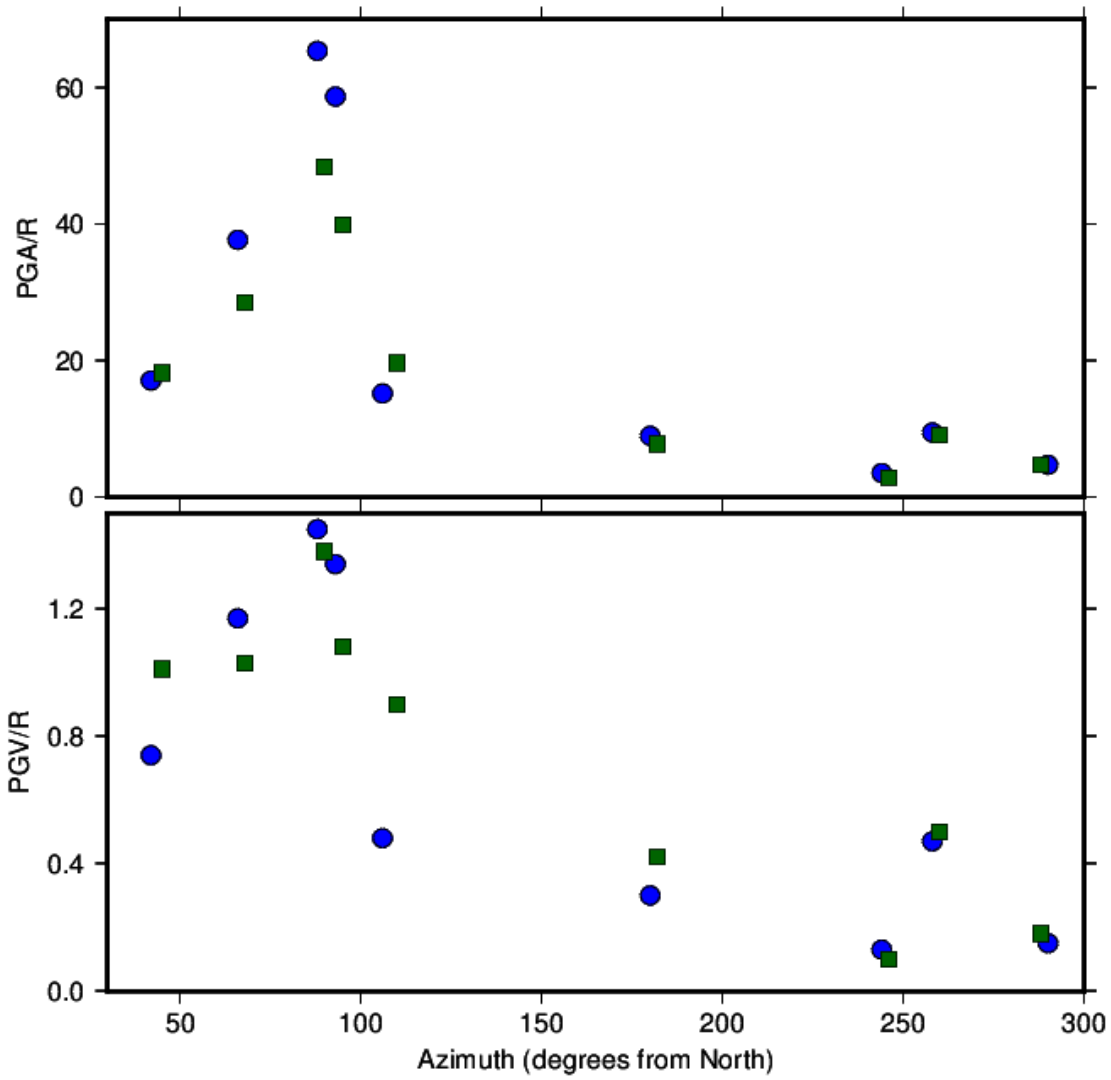

Figure 4. Normalized PGA and PGV values with respect to hypocentral distance, R, as a function of azimuth from north. Mw 4.3 is shown as blue circles, Mw 4.4 is shown as green squares.

Table 1. Location and source parameters for the three events used in the EGF analysis

	Element event	Mw 4.3	Mw 4.4
Date	2025-08-22 09:21:59	2025-08-22 06:45:37	2026-01-19 23:06:56
Magnitude (Mw)	2.8	4.3	4.4
Depth (km)	3.9	4.0	4.0
Longitude / Latitude	-84.076 / 9.935	-84.076 / 9.939	-84.072 / 9.936
Strike / Dip / Slip	51 / 56 / -20	86 / 70 / -15	76 / 62 / -17

2.2 Empirical Green's Function Method

The empirical Green's function method relies on the assumption that the records from smaller events can be used to reconstruct a larger one as far as they both share similar focal mechanism and hypocentral locations. The rupture process is represented by a finite number of subfaults, *N*, that corresponds to what

195 Miyake et al. (2003) describe as a strong motion generation area (SMGA). A SMGA is a localized portion of the
196 fault plane that radiates high-frequency seismic energy and controls the generation of near-field strong
197 ground motions. It is characterized by relatively large slip, short rise time, and high stress drop compared to
198 the surrounding rupture area.

199 Irikura (1986) assumed an omega-squared model (Brune, 1970) to reconstruct the main event ("Mw 4.3"
200 and "Mw 4.4" in Table 1), U(t), as the summation of a smaller event (the "Element event" in Table 1), u(t),
201 distributed along a given number of subfaults, *N*. In his formulation, the waveform U(t) can be expressed as
202 follows,

203

204 $$U(t)=C\sum\sum\frac{r}{r_{ij}}F(t-t_{ij})\ *\ u(t) \quad (1)$$

205

206 $$t_{ij}=\frac{r_{ij}-r_o}{\beta}+\frac{\xi_{ij}}{V_R} \quad (2)$$

207

208 $$F(t)=\delta(t)+\frac{1}{n'}\sum\delta\left[t-(k-1)\frac{\tau}{(N-1)n'}\right] \quad (3)$$

209

210 where $u(t)$ is the ground-motion from the element event, r, r_{ij}, and r_o are the corresponding distances from
211 the site to the hypocenter, the site to the *(i,j)* subfault and from the site to the rupture starting point on the
212 fault plane (Fig. 5). ξ_{ij} corresponds to the distance between the starting point and the (*i,j*) subfault, β is the S-
213 wave velocity, V_r is the rupture velocity, τ is the riste time of the target event, C is the stress drop ratio
214 between the target and element event, and n' is an arbitrary integer number used to shift the artificial
215 periodicity to a frequency higher than that of interest. The asterisk in (1) denotes convolution in the time
216 domain.

217 From the spectral ratio between the observed records from the large and small event, Miyake et al.
218 (2003) proposed thee following equation for fitting a theoretical source model such that,

219 $$SSRF(f)=\frac{M_o}{m_o}\frac{1+\left(\frac{f}{f_a}\right)^2}{1+\left(\frac{f}{f_m}\right)^2} \quad (4)$$

where f_m and f_a correspond to the corner frequency of the large and small magnitude event respectively. If $f \to 0$ then

$$\frac{M_o}{m_o} = CN^3 \quad (5)$$

and when $f \to \infty$

$$\left(\frac{M_o}{m_o}\right)\left(\frac{f_m}{f_a}\right)^2 = CN \quad (6)$$

Then, the *N* and *C* constants can be obtained as,

$$N = \frac{f_a}{f_m} \quad (7)$$

$$C = \left(\frac{M_o}{m_o}\right)\left(\frac{f_m}{f_a}\right)^3 \quad (8)$$

For each station, the Fourier amplitude spectrum was calculated. We assumed an S-wave velocity, *Vs*, of 3.2 km/s and corrected the records by geometrical spreading and quality factor $Q(f) = 179 f^{0.5598}$ (Chavarría et al., 2023). We took the vectorial summation $O(f) = \sqrt{(NS(f)^2 + EW(f)^2)}$ of the horizontal compoents, *NS(f)* and *EW(f)*. The spectral ratios (Fig. 6) were then computed and a theoretical omega-squared model was fitted to the data using equation 4. The corner frequencies estimated from spectral ratios are very similar (8.1 and 7.8 Hz), justifying the use of a common EGF to better isolate source effects (e.g., Wen et al., 2014). Given the small size of the element event, we assumed that the width (*w*) and length (*l*) (Fig. 5) were equal, such that *dx=w=l*. Using the Brune (1970) circular crack model and a corner frequency of 7.95 Hz, the source radius was calculated as

$$r = 0.37\frac{Vs}{f_a} \quad (9)$$

The corresponding $dx = \sqrt{(A)}$= 0.26 km, where $A = \pi r^2$. For the Mw 4.3 event, we obtained N=3 and C=5.3, whereas for the Mw 4.4 event we obtained N=4 and C=3.2. A grid-search approach was used to determine the optimal rupture initiation point for each SMGA, as well as the rise time and rupture velocity.

3. Results

3.1 Waveform fitting

The observed (black) and synthetic (red) displacement, velocity, and acceleration waveforms for the Mw 4.3 and Mw 4.4 events are shown in Figure 7 and 8. The quality of the fitting varies among stations and between components. Several stations show agreement in both phase and amplitude, while others show minor discrepancies specially in the later portions of the waveforms, where the synthetics tend to under- or over-estimate secondary arrivals and coda amplitude (in particular at NS component for SUN6 in displacement and SCNE and SBEB). Component-dependent differences are also evident. Figure 9 shows how well the PGA, PGV, and PGD observed values adjust with the synthetic ones. In both events, the EW component seems to be the one with better fits.

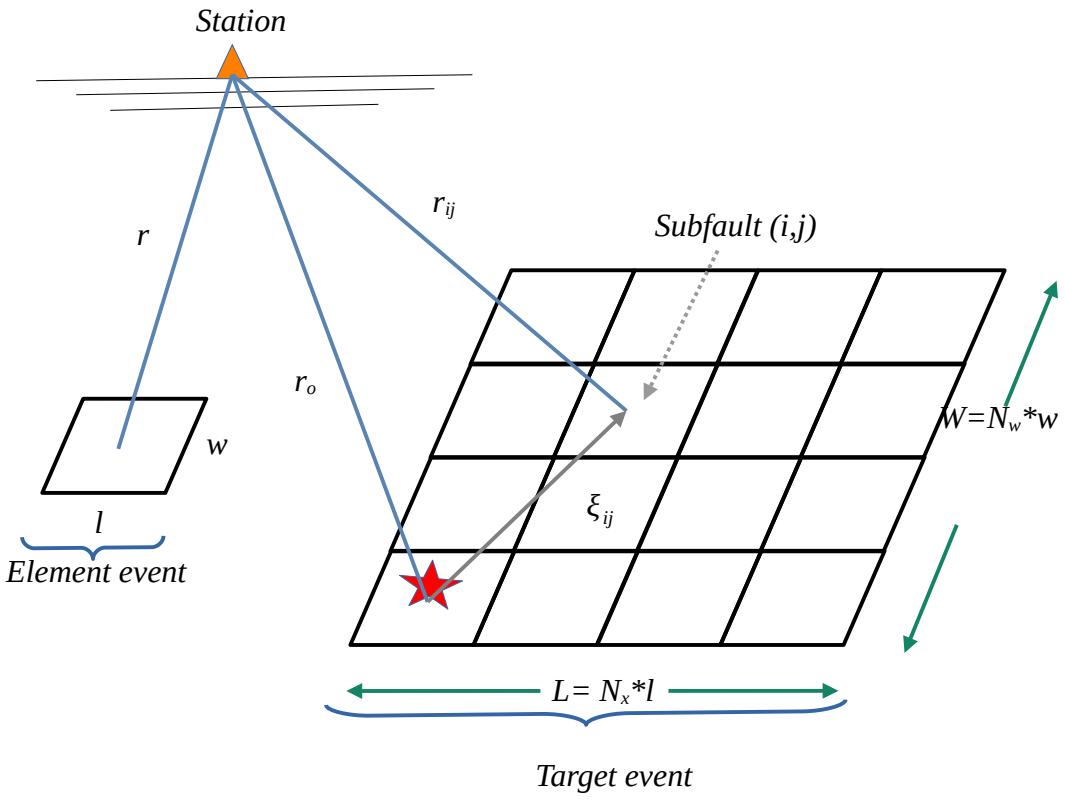

Figure 5. Schematic representation of the empirical Green's function method by Irikura (1986).

The element event's (M2.8) seismic moment was calcualted as 2.0E13 N-m; its corresponding stress drop was $\Delta\sigma = 2.77$ MPa. The SMGA's seismic moment was computed as $C\,N^3 m_o$ and the stress drop as $C\,\Delta\sigma$. Table 2 summarizes the parameters obtained during the inversion process for each earthquake. They indicate that the rupture processes were not identical even though the events magnitude and location were very similar.

For the Mw 4.3 event, the relatively small SMGA area (0.61 km^2), short rise time (0.06 s), and high stress drop (14.7 MPa) could be responsible for the impulsive character and strong high-frequency content of the observed acceleration records. The rupture initiation point at position (1,3), located toward the western portion of the SMGA (Fig. 10), could result in a rupture geometry that enhanced seismic radiation toward the east. This would explain the larger observed PGA and PGV values at eastern stations such as SUN6, SUN7, and SUNL, although peak amplitudes are slightly underestimated at the closest eastern stations, such as SION.

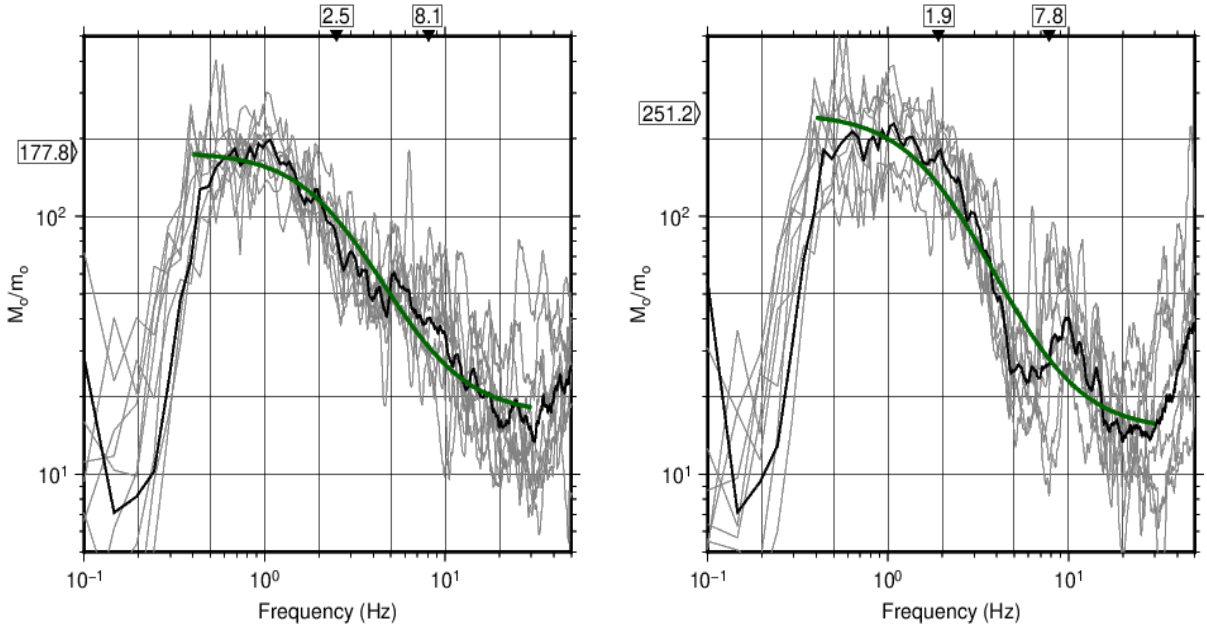

Figure 6. Single spectral ratios between the Mw 4.3 / M2.8 (left) and Mw 4.4 / M2.8 (right) events at the recording sites (gray lines). The corresponding corner frequencies are shown on top and the ratio between their seismic moments, M_o/m_o, on the left. The thick black line corresponds to the average and the green line to the least-squares fitting following equation 4.

Table 2. Source parameters from the EGF inversion.

	Mw 4.3	Mw 4.4
SMGA (km^2)	0.61	1.08
Number of sufaults	3x3	4x4
Rupture starting point	(1 , 3)	(2 , 4)
Rise time (s)	0.06	0.08
Seismic moment of SMGA (N-m)	2.86E15 (Mw 4.3)	4.61E15 (Mw 4.4)
Rupture velocity (km/s)	2.24 (0.70% of Vs)	2.85 (0.89% of Vs)
Stress drop (MPa)	14.70	9.98

On the contrary, the Mw 4.4 event has larger SMGA (1.08 km^2), longer rise time (0.08 s), and lower stress drop (9.98 MPa) that could lead to waveforms with slightly longer durations and smoother envelopes which are observed in displacement and velocity records. The rupture initiation point at (2,4) is deeper and

slightly shifted (Fig. 10) compared to that of the Mw 4.3 event. This could result in a different rupture propagation pattern within the SMGA that could produce subtle but systematic differences in waveform amplitude and timing, particularly at intermediate and eastern stations.

Figure 7. Waveform fitting between observed (black) and synthetic (red) data for both horizontal components in

290 displacement, velocity, and acceleration for event Mw 4.3.

291

292

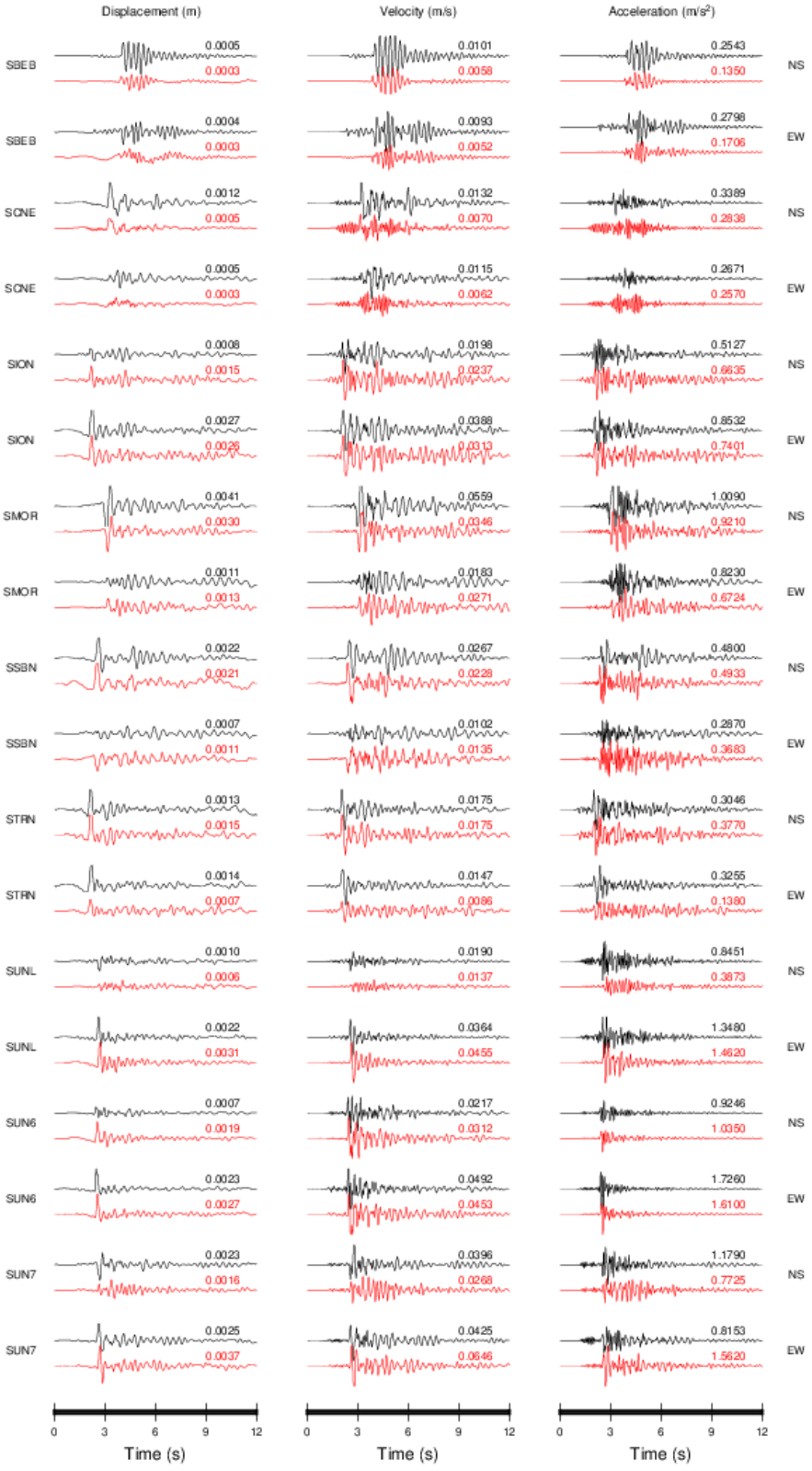

293 **Figure 8.** Waveform fitting between observed (black) and synthetic (red) data for both horizontal components in

displacement, velocity, and acceleration for event Mw 4.4.

3.2 Stress drop

Stress drop estimates for small to moderate earthquakes are commonly derived from spectral corner frequencies using circular crack models. Although these estimates exhibit wide variability, typical stress drop values for crustal earthquakes with magnitudes of approximately M3 – M4 generally cluster below ~10 MPa. For example, a spectral study of shallow earthquakes in Western Europe by Yen et al. (2024) reported a mean stress drop of ~8.6 MPa for events with M > 3, while Bora (2017) found median values of ~5.6–5.8 MPa for shallow crustal earthquakes in the same region. Similarly, Hardebeck and Aron (2009) reported a median stress drop of ~8.7 MPa for M1.0 – M4.2 earthquakes along the Hayward Fault in California.

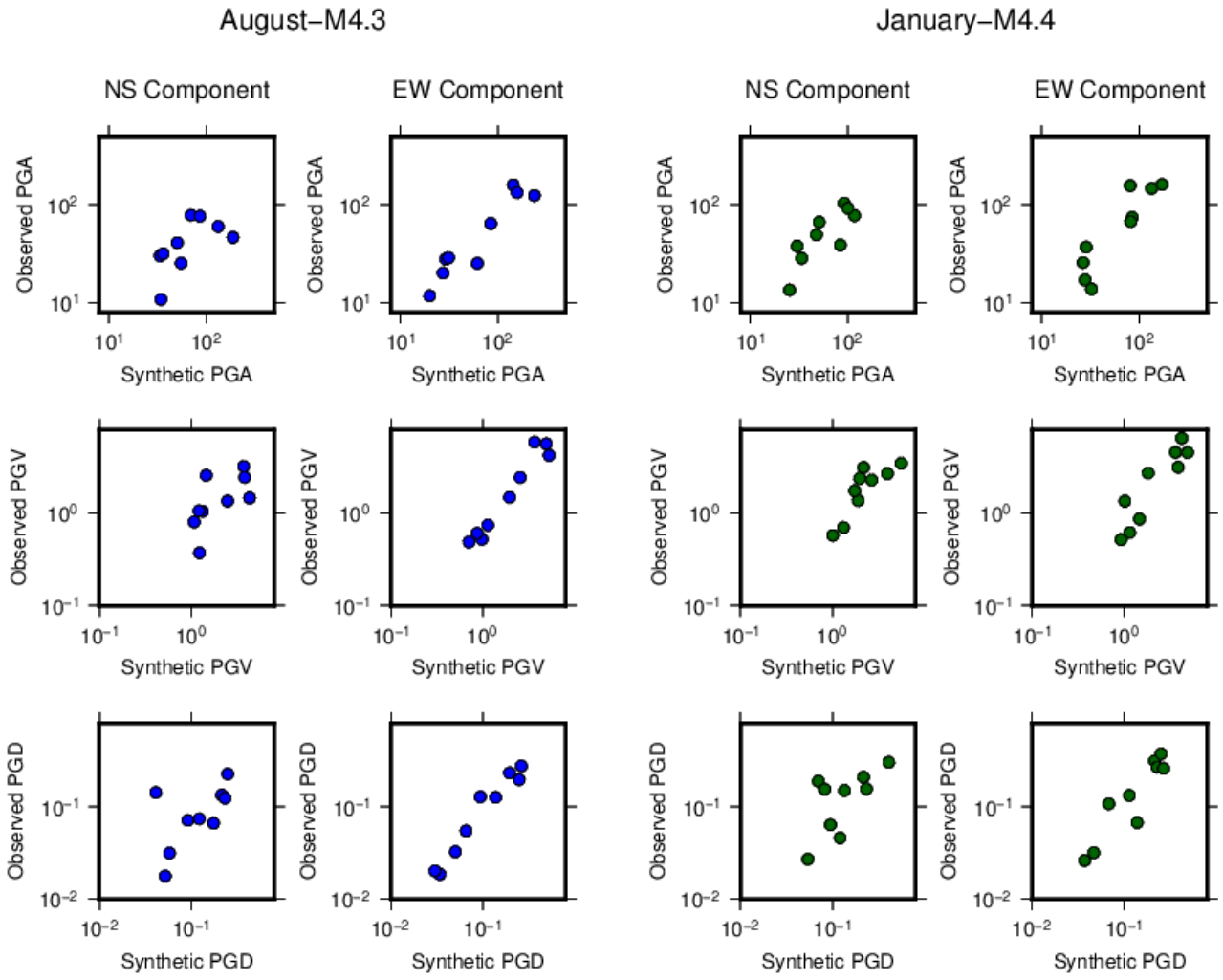

Figure 9. Comparison between observed vs synthetic peak ground displacement, velocity, and acceleration values for the Mw 4.3 (blue circles) and Mw 4.4 (green circles) events.

In contrast, the stress drops estimated in this study correspond to the SMGAs. As such, they represent effective stress drops associated with the high-slip, high-radiation portions of the rupture and are expected to be higher than stress drops inferred from whole-source models. Previous studies have shown that SMGA or asperity-based stress drops commonly exceed spectral estimates because they emphasize localized regions of concentrated slip and energy release (e.g., Miyake et al., 2003; Asano & Iwata, 2012). Within this context, the relatively high stress drop of the Mw 4.3 event (~14.7 MPa) is physically reasonable and consistent with the observed impulsive waveforms, whereas the lower stress drop of the Mw 4.4 event (~9.98 MPa), combined with its larger SMGA and longer rise time, probably explain the lower PGA and PGV values compared to the Mw 4.3 event.

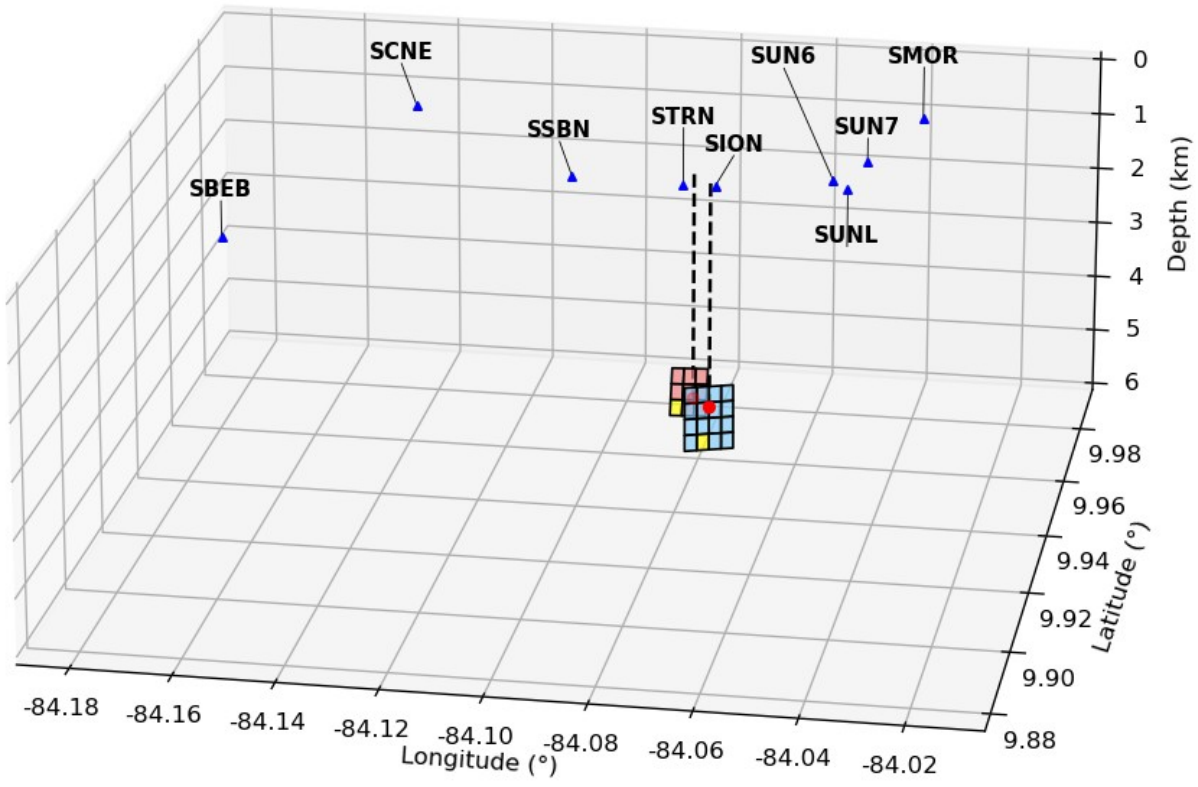

Figure 10. 3D figure showing the location of the SMGAs for the Mw 4.3 (red) and Mw 4.4 (blue) earthquakes. The rupture starting point is highlighted in yellow for both events. The red dot is the hypocenter and the dashed line its projection on the surface. The two earthquakes are located between the STRN and SION stations.

Wen et al. (2014) showed that two closely spaced blind-thrust earthquakes in the 2013 Nantou sequence, Taiwan, despite similar magnitudes and focal mechanisms, exhibited distinct strong-motion

characteristics associated with different SMGA stress drops (~14 MPa and ~9 MPa). Likewise, Somei et al. (2024) demonstrated for the 2018 Northern Osaka Prefecture earthquake that relatively high SMGA stress drops (~14–15 MPa) and rupture propagation within the SMGA were essential to reproducing observed azimuthal variations in PGA and PGV. This implies that even closely located earthquakes with different stress drops on a similar fault may generate different strong-motion patterns when their SMGA properties differ.

4. CONCLUSIONS

The following conclusions summarize the key findings from this study.

1. The Mw 4.3 and Mw 4.4 earthquakes were likely generated on the same fault or fault segment, as indicated by their similar focal mechanisms, hypocentral locations, and highly coherent observed waveforms from all stations that recorded the events. However, differences in rupture parameters obtained from the simulations confirm that their rupture processes were not identical.

2. Variations in waveform fittings, particularly in later phases and coda, suggest that local site effects, small-scale rupture heterogeneities, and limitations of the simplified source model could contribute to discrepancies between observed and synthetic records.

3. Source-related parameters—specifically SMGA size, stress drop, rise time, and rupture initiation location—could play a dominant role in controlling the amplitude, frequency content, and duration of observed ground motions for both events. The Mw 4.3 event is characterized by a smaller SMGA, shorter rise time, and higher effective stress drop. On the other hand, the Mw 4.4 event exhibits a larger SMGA, longer rise time, and lower stress drop.

4. A pronounced eastward amplification of ground motion is observed for both events, with PGA increasing significantly from western to eastern stations. Distance-normalized ground-motion measures confirm that this pattern is primarily source-driven rather than a result of attenuation or path effects. Also, despite the larger seismic moment of the second event, it does not systematically generate larger PGA or PGV values, probably highlighting the importance of stress drop and rupture geometry over moment alone.

5. Western stations show relatively uniform distance-normalized PGA and PGV values between the two events, suggesting more homogeneous radiation and attenuation. In contrast, eastern stations display greater variability, which may reflect directional source effects and differences in SMGA radiation.

352 6. The elevated SMGA stress drops estimated in this study are physically reasonable and consistent with
353 previous asperity-based studies, reinforcing that effective stress drops associated with high-slip regions can
354 exceed whole-source spectral estimates.

355 7. The occurrence of two moderate-magnitude earthquakes beneath a densely populated urban area,
356 producing strong spatial variability in ground motion over short distances, underscores the need to
357 incorporate source complexity and rupture directivity into seismic hazard assessments, even for moderate
358 events.

359
360
361 **Data availability statement.** Strong motion data is available at https://crsmd.lis.ucr.ac.cr/. A program of
362 the empirical Green's function method by Irikura (1986) can be provided upon request to the author.
363

364
365 **Acknowledgments.** Strong motion data for the 2025-2026 events was collected and maintained by
366 technical stuff from LISUCR Luis Navarro and Gustavo Poveda.

367

368 # References

369 Alonso-Henar, J., Montero, W., Martínez-Díaz, JJ, and Alvarez-Gómez, JA. (2013). The Aguacaliente fault, source
370 of the Cartago 1910 destructive earthquake (Costa Rica). *Terra Nova*, 25(5), 368-373.
371 https://doi.org/10.1111/ter.12045.
372 Asano, K., Iwata, T. (2012). Source model for strong ground motion generation in the frequency range 0.1–10
373 Hz during the 2011 Tohoku earthquake. *Earth Planets Space,* 64, 1111–1123.
374 https://doi.org/10.5047/eps.2012.05.003.
375 Barquero, R. (2009). El terremoto de Cinchona del jueves 8 de enero de 2009. *Rev. Geol. Am. Cent.,* 40, 91–95.
376 https://doi.org/10.15517/rgac.v0i40.4188.
377 Benito, M.B., Arroyo-Solórzano, M., Climent, Á., Montero, W., Alvarado, G.E., López, A., García-Lanchares, C.,
378 Marchamalo, M., Ornelas, A., Hernández-Rubio, O., Quirós, L. (2025). Seismic hazard scenarios for the
379 city of San José, Costa Rica: Evaluation of critical ruptures on nearby faults. *Earthq. Spectra,* 2025*,* 41(3),
380 2335–2370. https://doi.org/10.1177/87552930251319736.
381 Bora, S.S., Cotton, F., Scherbaum, F., et al. (2017). Stochastic source, path and site attenuation parameters and
382 associated variabilities for shallow crustal European earthquakes. *Bull. Earthq. Eng.*, 2017, 15, 4531–4561.
383 https://doi.org/10.1007/s10518-017-0167-x.
384 Brune, J.N. (1970). Tectonic stress and the spectra of seismic shear waves from earthquakes. *J. Geophys. Res.*,
385 75, 4997–5009.
386 Chavarría, N., Yokoi, T., Hayashida, T. (2023). Strong motion estimation in Costa Rica at non-record sites using
387 spectral inversion method. *J. Seismol.,* 27, 305–324. https://doi.org/10.1007/s10950-023-10137-9.
388 Climent, Á., Rojas, W., Alvarado, G. E. y Benito, B. (2008). Proyecto Resis II: Evaluación de la amenaza sísmica
389 en Costa Rica. UPM, NOR- SAR, San José, Costa Rica.,
390 https://rsn.ucr.ac.cr/images/Biblioteca/Informes_sismos/amenaza_Sísmica_cr.pdf. Accessed 05 Feb
391 2026.
392 Fernández, M., Montero, W. (2002). Fallamiento y sismicidad del área entre Cartago y San José, Valle Central
393 de Costa Rica. *Rev. Geol. Am. Cent.,* 2002*,* 26, 25–37. https://doi.org/10.15517/rgac.v0i26.8528.
394 Hardebeck, J.L., Aron, A. (2009). Earthquake stress drops and inferred fault strength on the Hayward Fault,
395 East San Francisco Bay, California. *Bull. Seismol. Soc. Am.,*99,1801–1814.

396 https://doi.org/10.1785/0120080242.
397 Hardebeck, J.L., Shearer, P.M. (2002). A new method for determining first-motion focal mechanisms. *Bull.*
398 *Seismol. Soc. Am.*, 92(6), 2264–2276. https://doi.org/10.1785/0120010200.
399 Hidalgo-Leiva, D., Linkimer, L., Arroyo, I., Arroyo-Solórzano, M., et al. (2022). The 2022 seismic hazard model
400 for Costa Rica. *Bull. Seismol. Soc. Am.,* 113(1), 23–40. https://doi.org/10.1785/0120220119.
401 Irikura, K. (1986). Prediction of strong acceleration motion using empirical Green's function. In: *Proc. 7th Japan*
402 *Earthquake Engineering Symposium*, Tokyo, pp. 151–156.
403 Lomax, A., J. Virieux, P. Volant and C. Berge-Thierry. Probabilistic Earthquake Location in 3D and Layered
404 Models. In: Thurber C.H., Rabinowitz N. (eds) (2000). Advances in Seismic Event Location, Modern
405 Approaches in Geophysics, 18, Springer, Dordrecht, doi:10.1007/978-94-015-9536-0_5.
406 Miyake, H., Iwata, T., Irikura, K. (2003). Source characterization for broadband ground-motion simulation:
407 Kinematic heterogeneous source model and strong motion generation area. *Bull. Seismol. Soc. Am.* , 93,
408 2531–2545. https://doi.org/10.1785/0120020183.
409 Montero, W., Miyamura, S. (1981). Distribución de intensidades y estimación de los parámetros focales de los
410 terremotos de Cartago de 1910, Costa Rica, América Central. *Inf. Sem. IGN* , 1981**,** (2), 9–34.
411 Moya, A., Pinzón, L.A., Schmidt-Díaz, V., Hidalgo-Leiva, D., Beneit, L. (2020). A strong-motion database of Costa
412 Rica: 20 years of digital records. *Seismol. Res. Lett.* ,2020, 91, 3407–3416.
413 https://doi.org/10.1785/0220200036.
414 Moya, Aaron. (2024). The MASLIS: A five-year review of Costa Rica's near real-time seismic intensity processing
415 system. Annals of Geophysics. 67. S552. 10.4401/ag-9137.
416 OVSICORI-UNA, Reporte de actividad sísmica: Estudio preliminar de la actividad sísmica en el centro de San
417 José entre agosto de 2025 y enero de 2026.
418 https://www.ovsicori.una.ac.cr/index.php/sismologia/informes-y-boletines/boletines-sismologia?
419 download=1295:reporte-de-actividad-Sísmica-estudio-preliminar-de-la-actividad-Sísmica-en-el-centro-
420 de-san-José-entre-agosto-de-2025-y-enero-de-2026 , Accessed 05 Feb 2026.
421 Peraldo, G., Montero, W. (1999). *Sismología histórica de América Central*. Instituto Panamericano de Geografía e
422 Historia–UCR, 348 pp.
423 Quesada Román, A., Barrantes Castillo, G. (2016). Procesos de ladera cosísmicos del terremoto de Cinchona
424 (Costa Rica) del 8 de enero de 2009 (Ms = 6.2). *Cuad. Geogr.* , 25(1), 217–232.
425 RSN, Sismos en San José, enero de 2026. https://rsn.ucr.ac.cr/index.php/actividad-Sísmica/reportes-sismicos/
426 sismo-en-san-José-19-de-enero-de-2026, Accessed 05 Feb 2026.
427 Somei, K., Guo, Y., Yoshida, K., Akazawa, T., Nishimura, T., Miyakoshi, K., Irikura, K. (2024). Reproductions of
428 strong ground motions during the 2018 Northern Osaka Prefecture earthquake using the empirical
429 Green's function method. *Jpn. Geotech. Soc. Spec. Publ.,* 10 (60), 2465–2468.
430 https://doi.org/10.3208/jgssp.v10.P2-22
431 U.S. Geological Survey (USGS), n.d. Why do USGS earthquake magnitudes differ from those published by other
432 agencies? available at https://www.usgs.gov/faqs/why-do-usgs-earthquake-magnitudes-differ-those-
433 published-other-agencies. Accessed 05 Feb 2026.
434 Yen, M.-H., Bindi, D., Oth, A., et al. (2024). Source parameters and scaling relationships of stress drop for
435 shallow crustal seismic events in Western Europe. *J. Seismol.*, 28, 63–79. https://doi.org/10.1007/s10950-
436 023-10188-y
437 Wen, Y.-Y., Miyake, H., Yen, Y.-T., Irikura, K., Ching, K.-E. (2014). Rupture directivity effect and stress
438 heterogeneity of the 2013 Nantou blind-thrust earthquakes, Taiwan. *Bull. Seismol. Soc. Am.,* 104(6), 2933–
439 2942. https://doi.org/10.1785/0120140109
440
441
442
443
444
445 ***CORRESPONDING AUTHOR: Aaron**
446 **MOYA**,
447 Laboratorio de Ingeniería Sísmica, Universidad de Costa Rica, COSTA RICA

Aaron Moya

e-mail:
cesar.moya@ucr.ac.cr